Journal of Fluids and Structures (2001) **15,** 235–253
doi:10.1006/jfls.2000.0339, available online at http://www.idealibrary.com on IDEAL®

INLET GUIDE VANE WAKES INCLUDING ROTOR EFFECTS

R. T. Johnston and S. Fleeter

School of Mechanical Engineering, Purdue University, West Lafayette, IN 47907, U.S.A.

(Received 29 June 1998, and in final form 3 August 2000)

Fundamental experiments are described directed at the investigation of forcing functions generated by an inlet guide vane (IGV) row, including interactions with the downstream rotor, for application to turbomachine forced response design systems. The experiments are performed in a high-speed research fan facility comprised of an IGV row upstream of a rotor. IGV-rotor axial spacing is variable, with the IGV row able to be indexed circumferentially, thereby allowing measurements to be made across several IGV wakes. With an IGV relative Mach number of 0·29, measurements include the IGV wake pressure and velocity fields for three IGV-rotor axial spacings. The decay characteristics of the IGV wakes are compared to the Majjigi and Gliebe empirical correlations. After Fourier decomposition, a vortical–potential gust splitting analysis is implemented to determine the vortical and potential harmonic wake gust forcing functions both upstream and downstream of the rotor. Higher harmonics of the vortical gust component of the IGV wakes are found to decay at a uniform rate due to viscous diffusion.

1. INTRODUCTION

Inlet guide vane wakes interacting with a downstream rotor are known to contribute to aerodynamic losses, pure tone noise, and rotor blade vibrations that may lead to high cycle fatigue, resulting in decreased component life. In this regard, wake–blade row interactions are the most common and least understood source of unsteady aerodynamic excitation causing blade row vibrations. Currently, linearized forced response predictions are utilized in HCF design systems. These are typically based on linearized two-dimensional inviscid cascade flow analyses that consider each wake harmonic gust forcing function independently. These gust-forcing functions consist of two components: potential and vortical disturbances.

Potential disturbances, a result of blade thickness and lifting properties, are an inviscid effect and extend both upstream and downstream. They decay exponentially with distance in a subsonic flow, but do not decay in a supersonic flow. Thus, when the through flow is subsonic, the decaying potential field is significant for closely spaced blade rows found in modern and advanced turbomachines. Vortical disturbances, convecting with the mean flow, result from the viscous action at the blade surface. Fundamental vortical gust forcing functions have been considered by Henderson & Fleeter (1992); also, combined vortical–potential gust forcing functions have been considered by Manwaring & Wisler (1992) and Feiereisen *et al.* (1993).

Currently used wake forcing-function models are typically empirical or semi-empirical and based on far-wake steady flow data, often incompressible, from single isolated airfoil rows. As a result, conventional wake forcing-function models are significantly limited with regard to forced response prediction in modern closely spaced blade rows. Empirical wake

0889–9746/01/020235 + 19 $35.00/0

models include those of Mugridge & Morfey (1971), and Lakshminarayana & Davino (1980), each of whom developed separate equations for the near- and far-wake regions. Majjigi & Gliebe (1984) developed a linear rational model to describe wake behavior, whereby only one equation is required for both the near- and far-wake regions.

Observations on the effect of stationary vane wakes that had passed through a rotating blade row on downstream blade rows are reported by Schmidt & Okiishi (1977). It was seen that the wake of a stator positioned in the deficit from the upstream stator had a larger deficit than if it was positioned between the incoming stator wakes. The implications for a multistage machine are considerable if the stationary blade rows are incorrectly positioned. Rotor blade wake velocity deficits have been found to decrease in the region of an upstream stator velocity deficit (Walker & Oliver 1972; Johnston *et al.* 1994). Walker & Oliver (1972) argue that this phenomenon can be exploited to effect a reduction in sound level at the blade passage frequency by spanwise bending of the downstream stator so that the stator blade leading edge meets the rotor wakes in this reduced deficit region.

There is thus a well-defined industry-wide need for relevant turbomachinery wake data that include potential effects associated with downstream closely spaced blade rows. Namely, the development of accurate flow-induced vibration design system models for application to modern and advanced turbomachinery that feature closely spaced airfoil rows requires wake models based on data that includes multistage interaction effects.

This paper addresses this need for turbomachinery wake data appropriate for flow-induced forced response design analysis of advanced blade rows, both near- and far-wake, that includes airfoil row interaction effects. This is accomplished through fundamental experiments performed in the Purdue Research Axial Fan Stage directed at investigating the aerodynamic forcing functions generated by an IGV row, including interactions with the downstream rotor. This facility, comprised of an IGV row and a rotor, is ideal for the experimental study of these wake forcing functions because it is large enough for the necessary high-quality measurements, the IGV-rotor axial spacing is variable, and the IGV row can be indexed circumferentially, thereby enabling inlet guide vane wakes to be measured with stationary probes. With an IGV relative Mach number of 0·29, the IGV wake pressure and velocity fields are measured with hot-film anemometers and total pressure probes. First, the decay characteristics of the IGV wakes for three IGV-rotor axial spacing values are compared to empirical correlations. After Fourier decomposition, a vortical–potential gust splitting analysis is then implemented to determine the vortical and potential harmonic wake gust forcing functions both upstream and downstream of the rotor. Results of the vortical–potential splitting analysis are studied to assess the effects of IGV axial spacing and IGV–rotor interactions.

2. AXIAL FAN FACILITY

The Purdue Research Axial Fan facility features a 30·48 cm (12 in) diameter, 2/3 hub-tip ratio design compressor rotor that is integral with the shaft. The drive system consists of a 300 horsepower AC motor driving a magnetic clutch with a variable speed output that drives a gearbox. Eighteen inlet guide vanes introduce swirl into a 19-blade axial flow rotor (Figure 1). The inlet guide vanes and rotor blades were designed with NACA 65 series profiles on circular arc meanlines. The adjustable inlet guide vanes have a nominal 10% thickness with a chord varying from 35·5 mm (1·40 in) at the hub to 53·3 mm (2·10 in) at the tip, to yield a solidity of 1. The IGV twist distribution produces a free vortex whirl into the rotor. Rotor blade sections have a 10–6% hub-to-tip thickness taper, with a chord of 50·8 mm (2·00 in). For these experiments, axial IGV-to-rotor spacing to chord ratios of $Z/C_R = 0{\cdot}68$, 0·93, and 1·18 are investigated. The IGV row is indexed circumferentially,

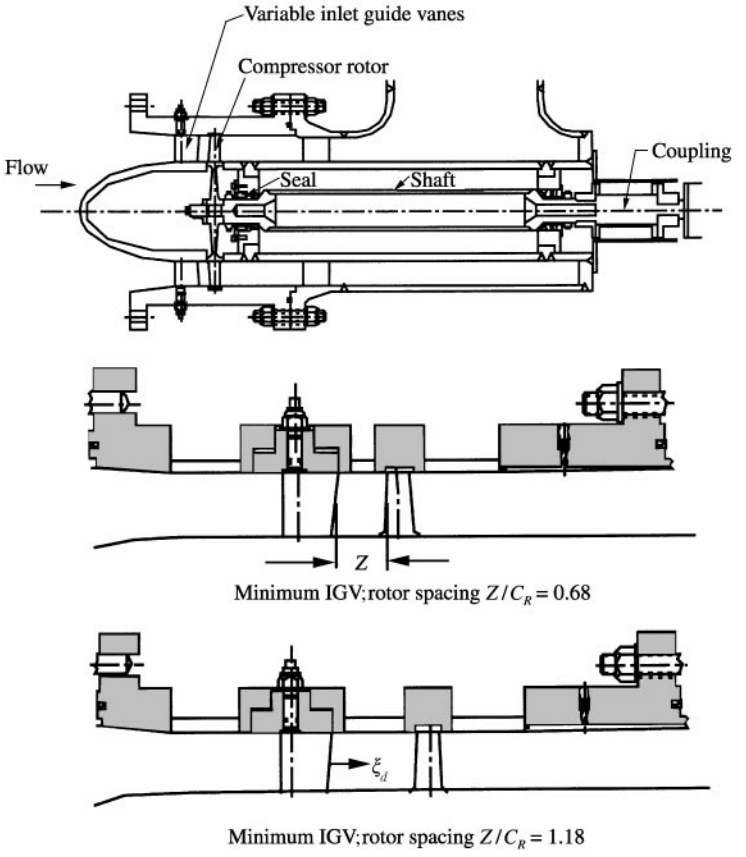

Figure 1. Research fan stage cross-section and spacing detail.

thereby enabling the IGV wake measurements to be made without circumferential probe traverses upstream and downstream of the rotor. The turbulence intensity measured 26 mm upstream of the inlet guide vanes is 2·5%. The compressor is operated at 10000 rpm for all tests giving a total pressure ratio of 1·08 and typical mass flow rates of 3·8 kg/s (8·4 lb/s).

Midspan velocity and total pressure are measured both upstream and downstream of the rotor with hot-film anemometers and total pressure probes designed to access the confined regions downstream of the IGV row and the rotor. An Endevco piezoresistive pressure transducer with a sensitivity of 59·85 mV/psi and a frequency response of 70 kHz has been installed into the stainless-steel probe body. This design is capable of $\pm 17^\circ$ misalignment to the flow with less than 1% error in total pressure. The crossed hot-film has a measurement area of 50·8 μm × 1·0 mm, with absolute velocity magnitude and flow angle errors estimated to be less than 4% and 0·5°, respectively. All probes are set to minimize flow angle deviations from the probe axis.

3. DATA ACQUISITION

At each circumferential location of the IGV, the time mean velocity and total pressure are measured to determine their downstream spatial variation. The measurements are taken at 1° increments in the free stream and at 0·1° increments while in the wake. Wake regions are identified by first taking a traverse of two inlet guide vane passages with the coarse

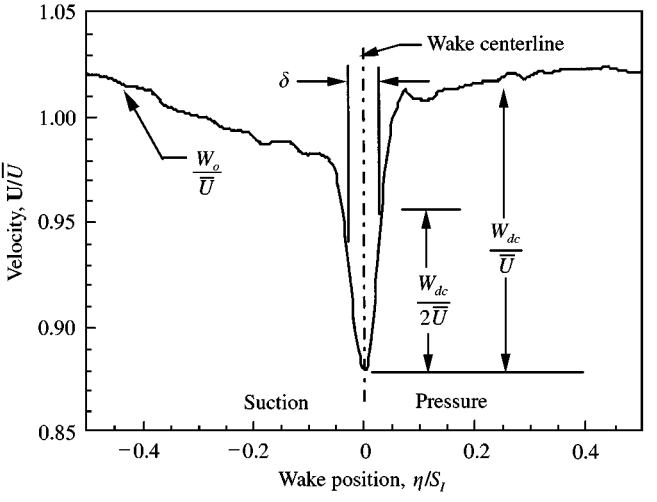

Figure 2. Typical IGV wake velocity deficit.

circumferential increments. Wake regions, once identified, are then resolved by taking measurements at smaller increments across each of the two wakes. Time-mean signals at each IGV azimuthal location are determined by taking the average of measurements of 80 rotor revolutions sampled at 1900 points per revolution for each data channel. These measurements of the spatial variation of velocity and total pressure are then used to calculate the spatial variations in static pressure assuming isentropic flow. The Fourier components of these spatial traces are numerically determined using Fourier Transform software after interpolating the data to a uniform spacing using a cubic spline fit. Traverses are exactly two IGV passages, eliminating frequency leakage problems in the Fourier analysis. The wakes from the two IGVs were in good agreement upstream of the rotor, whereas downstream of the rotor the variations were, understandably, more noticeable.

4. WAKE CORRELATION

The IGV wake decay characteristics are determined and correlated with the empirical correlations developed by Majjigi & Gliebe (1984) for the semi-wake width δ, and the wake centerline velocity defect W_{dc} (Figure 2). The correlation equations are

$$\frac{\delta}{C_I} = \frac{0{\cdot}2375(s/C_I)C_D^{0{\cdot}125} + 0{\cdot}034125}{0{\cdot}357(s/C_I)C_D^{0{\cdot}125} + 1{\cdot}0},$$
$$\frac{W_{dc}}{W_o} = C_D^{0{\cdot}25}\frac{0{\cdot}3675(s/C_I) + 1{\cdot}95}{7{\cdot}65(\mathrm{s/C}_I) + 1{\cdot}0}, \tag{1}$$

where δ is the semi-wake width, C_I is the IGV blade chord, s is the streamwise distance from the IGV trailing edge, C_D denotes airfoil section drag coefficient, and W_{dc} and W_o are the wake centerline velocity defect and free-stream velocity, respectively.

5. VORTICAL-POTENTIAL GUST SPLITTING ANALYSIS

The two-dimensional inviscid flow (Figure 3), is assumed to be compressible, isentropic, and composed of an absolute mean velocity $\bar{\mathbf{U}}$ with superimposed small velocity $\mathbf{w}$ and static

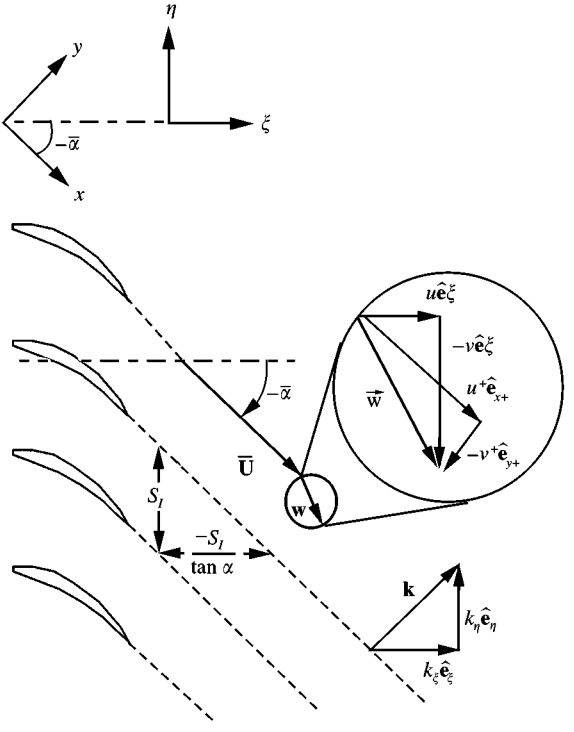

Figure 3. Model flow field.

pressure spatial perturbations p. The linearized continuity and momentum equations are

$$\frac{1}{c_0^2}\frac{\bar{\mathrm{D}}p}{\mathrm{D}t} + \bar{\rho}\nabla\cdot\mathbf{w} = 0, \qquad \bar{\rho}\frac{\bar{\mathrm{D}}\mathbf{w}}{\mathrm{D}t} + \nabla p = 0, \tag{2}$$

where an overbar indicates a mean value, c_0 is the speed of sound, and $\bar{\mathrm{D}}/\mathrm{D}t = \partial/\partial t + \bar{U}\,\partial/\partial x$.

5.1. Vortical-Potential Splitting

The perturbation velocity field is split into vortical and potential gust components per Goldstein's (1978) splitting theorem so that

$$\mathbf{w} = \mathbf{w}_v + \mathbf{w}_p, \tag{3}$$

where the vortical and potential velocity gusts satisfy the following equations:

$$\frac{\bar{\mathrm{D}}\mathbf{w}_v}{\mathrm{D}t} = 0, \qquad \nabla\cdot\mathbf{w}_v = 0, \tag{4}$$

$$\rho\frac{\bar{\mathrm{D}}\mathbf{w}_p}{\mathrm{D}t} = -\nabla p, \qquad \frac{1}{\rho c_0^2}\frac{\bar{D}p}{\mathrm{D}t} = -\nabla\cdot\mathbf{w}_p, \qquad \nabla\times\mathbf{w}_p = \mathbf{0}. \tag{5}$$

The forcing function is thus analyzed harmonically as a Fourier series of individual vortical and potential gusts:

$$\mathbf{w}(\mathbf{x}, t) = \sum\{\mathbf{w}_{vn}(\mathbf{x}) + \mathbf{w}_{pn}(\mathbf{x})\}\,\mathrm{e}^{\mathrm{i}n\omega t},$$

where $\mathbf{w}_{vn}(\mathbf{x})$ and $\mathbf{w}_{pn}(\mathbf{x})$ are the nth-harmonic vortical and potential gusts, respectively. The spatial coordinates are $\mathbf{x} = \xi\hat{\mathbf{e}}_\xi + \eta\hat{\mathbf{e}}_\eta$, where ξ and η are the axial and tangential components, and $\hat{\mathbf{e}}_\xi$ and $\hat{\mathbf{e}}_\eta$ are unit vectors.

5.2. Vortical Gust

Spatial periodicity shows that the gust wavenumber vector $\mathbf{k}$ must be perpendicular to the IGV mean flow exit velocity vector $\bar{\mathbf{U}}$.

$$\mathbf{k} \cdot \bar{\mathbf{U}} = 0, \tag{6}$$

where $\mathbf{k} = k_\xi\hat{\mathbf{e}}_\xi + k_\eta\hat{\mathbf{e}}_\eta$, k_ξ and k_η are the axial and tangential wavenumbers, and $\bar{\mathbf{U}} = \bar{U}(\cos\bar{\alpha}\hat{\mathbf{e}}_\xi + \sin\bar{\alpha}\hat{\mathbf{e}}_\eta)$ with $\bar{U}$ and $\bar{\alpha}$ denoting the flow velocity and angle, respectively.

Periodicity requirements determine the tangential wavenumber k_η, i.e. the flow is spatially periodic, repeating every inlet guide vane spacing. The axial wavenumber k_ξ is then determined from equation (6). Thus,

$$k_\eta = \frac{2\pi}{S_I}, \qquad k_\xi = -k_\eta \tan\bar{\alpha}. \tag{7}$$

The vortical gust convects with the mean flow $\bar{\mathbf{U}}$, i.e. $\mathrm{D}\bar{\mathbf{w}}_y/\mathrm{D}t = \mathbf{0}$, expressed as

$$\mathbf{w}_{vn} = \mathbf{w}_{vn}^{+} \exp\{-in\mathbf{k}\cdot(\mathbf{x} - \bar{\mathbf{U}}t)\}, \tag{8}$$

where $\mathbf{w}_{vn}^{+}$ is the nth-harmonic vortical gust amplitude vector.

This relationship and $\nabla \cdot \mathbf{w}_v = 0$ relate the wavenumber vector and the gust amplitude vector, such that the gust is oriented in a direction normal to $\mathbf{w}_{vn}$,

$$\mathbf{k} \cdot \mathbf{w}_{vn}^{+} = 0 \qquad \text{so that } \mathbf{w}_{vn} \perp \mathbf{k}. \tag{9}$$

Combining this condition with equation (6) shows that the vortical gust amplitude vector must be parallel to the mean velocity,

$$\mathbf{w}_{vn}^{+} \| \bar{\mathbf{U}}. \tag{10}$$

Denoting the complex constant of proportionality between these two constant vectors by D_n^* and noting that $\bar{\mathbf{U}} = \bar{U}(\cos\bar{\alpha}\hat{\mathbf{e}}_\xi + \sin\bar{\alpha}\hat{\mathbf{e}}_\eta)$ results in

$$\mathbf{w}_{vn} = D_n^* \bar{U}(\cos\bar{\alpha}\hat{\mathbf{e}}_\xi + \sin\bar{\alpha}\hat{\mathbf{e}}_\eta)\exp\{-in\mathbf{k}\cdot\mathbf{x}\}. \tag{11}$$

The vortical gust thus propagates unattenuated in the direction of the gust wavenumber vector $\mathbf{k}$. The dimensionless vortical gust can now be expressed as

$$\frac{\mathbf{w}_{vn}}{\bar{U}} = D_n^*(\cos\bar{\alpha}\hat{\mathbf{e}}_\xi + \sin\bar{\alpha}\hat{\mathbf{e}}_\eta)\exp\{-in\mathbf{k}\cdot\mathbf{x}\}. \tag{12}$$

5.3. Potential Gust

The potential gust $\mathbf{w}_p$ must satisfy $\nabla \times \mathbf{w}_p = \mathbf{0}$ and, therefore, can be derived from a potential function, $\mathbf{w}_p = \nabla\phi_p$. The perturbation potential is related to the pressure perturbation p through the unsteady Bernoulli equation. Substituting these relations into equation (2) yields the following perturbation velocity potential equation:

$$\frac{1}{c_0^2}\frac{\bar{\mathrm{D}}}{\mathrm{D}t}\left(\frac{\bar{\mathrm{D}}\phi_p}{\mathrm{D}t}\right) - \nabla^2\phi_p = 0. \tag{13}$$

Since the flow is steady, the potential gust can be determined from the steady form of this equation. This has solutions

$$\phi_{pn} = A_n \exp\{n(\chi k_\eta \xi - \mathrm{i} k_\eta \eta)\}, \tag{14}$$

where $\chi = \{ -\mathrm{i}M^2 \sin\bar{\alpha}\cos\bar{\alpha} \pm \sqrt{1 - M^2}\}/(1 - M^2\cos^2\bar{\alpha})$ is the axial decay factor and A_n is a complex constant.

Two values of χ exist, depending on the sign of the radical in the numerator. A downstream-going potential perturbation caused by an upstream airfoil row decays in the positive axial direction, so the minus sign is chosen. In the case of an upstream-going potential perturbation from a downstream airfoil row, the potential perturbation decays in the negative axial direction, so the plus sign is chosen. Thus, the potential gust is spatially periodic in the tangential direction but decays exponentially in the axial direction. The direction of this axial decay depends on whether an upstream or downstream blade row is being analyzed.

The potential static pressure perturbation is found from the unsteady Bernoulli equation.

$$p_{pn} = \rho A_n \bar{U} n k_\eta (-\chi\cos\bar{\alpha} + \mathrm{i}\sin\bar{\alpha}) \exp\{n(\chi k_\eta \xi - \mathrm{i} k_\eta \eta)\}. \tag{15}$$

Defining a dimensionless potential gust coefficient permits the potential static pressure and velocity spatial perturbations to be expressed in dimensionless form:

$$\frac{p_{pn}}{\rho \bar{U}^2} = A_n^* (-\chi\cos\bar{\alpha} + \mathrm{i}\sin\bar{\alpha}) \exp\{n(\chi k_\eta \xi - \mathrm{i} k_\eta \eta)\}, \tag{16}$$

$$\frac{\mathbf{w}_{pn}}{\bar{U}} = A_n^* (\chi \hat{\mathbf{e}}_\xi - \mathrm{i}\hat{\mathbf{e}}_\eta) \exp\{n(\chi k_\eta \xi - \mathrm{i} k_\eta \eta)\}. \tag{17}$$

5.4. Combined Vortical–Potential Gusts

The vortical and potential gusts are described in terms of their harmonics as follows:

$$\frac{\mathbf{w}_y}{\bar{U}} = (\cos\bar{\alpha}\hat{\mathbf{e}}_\xi + \sin\bar{\alpha}\hat{\mathbf{e}}_\eta) \sum D_n^* \exp\{-\mathrm{i}n\mathbf{k}\cdot\mathbf{x}\}, \tag{18}$$

$$\phi_p = \bar{U} \sum \frac{A_n^*}{n k_\eta} \exp\{n(\chi k_\eta \xi - \mathrm{i} k_\eta \eta)\}. \tag{19}$$

Thus, the linear theory combined vortical–potential gust is described by the complex vortical and potential gust coefficients D_n^* and A_n^*. Note that, except for D_n^* and A_n^*, which must be determined experimentally, the gust coefficients are completely specified.

5.5. Experimental Determination of D_n^* & A_n^*

The potential gust $\mathbf{w}_{pn}$ is irrotational. Hence, the vorticity $\boldsymbol{\gamma}_{pn}$ is zero, $|\boldsymbol{\gamma}_{pn}| = |\nabla \times \mathbf{w}_{pn}| = 0$, and p_{pn} is given in equation (16). The potential gust thus manifests itself in both static pressure and velocity spatial perturbations, but not in the vorticity perturbation. The vorticity of the vortical gust is $|\boldsymbol{\gamma}_{vn}| = |\nabla \times \mathbf{w}_{vn}| = D_n^* (\mathrm{i}n k_\eta \bar{U}/\cos\bar{\alpha}) \exp\{-\mathrm{i}n\mathbf{k}\cdot\mathbf{x}\}$, and there is no corresponding static pressure perturbation. This vortical gust component, therefore, manifests itself in a vorticity perturbation, but not in the static pressure perturbation.

The spatial static pressure perturbation is dependent only on the potential gust. At the measurement location defined by $(\xi, \eta) = (0, 0)$, the potential gust coefficient A_n^*, computed

explicitly from the calculated static pressure, is

$$A_n^* = \frac{p_{mn}}{\rho \bar{U}^2(-\chi \cos\bar{\alpha} + \mathrm{i}\sin\bar{\alpha})}, \tag{20}$$

where p_{mn} is the measured nth-harmonic static pressure spatial perturbation.

This measured static pressure spatial nonuniformity may be caused by both downstream- and upstream-going potential perturbations. Physical location dictates which solution is selected, with an appropriate value of χ.

The potential gust velocity perturbation, calculated using equation (17), is then subtracted from the measured velocity spatial non-uniformity to yield a difference velocity perturbation

$$\mathbf{w}_{dn} = u_{dn}\hat{\mathbf{e}}_\xi + v_{dn}\hat{\mathbf{e}}_\eta = (u_{mn} - u_{pn})\hat{\mathbf{e}}_\xi + (v_{mn} - v_{pn})\hat{\mathbf{e}}_\eta. \tag{21}$$

Since the vorticity of the potential component is zero, the perturbation of the velocity difference has the same vorticity as the measured gust. The linear theory vortical gust coefficient is thus calculated from this difference velocity perturbation,

$$D_n^* = \frac{1}{\bar{U}}(u_{dn}\cos\bar{\alpha} + v_{dn}\sin\bar{\alpha}). \tag{22}$$

Axial and tangential velocity components are then used to compute the streamwise and transverse components of the vortical and potential velocity fields with the following coordinate transformation:

$$\begin{Bmatrix} u^+ \\ v^+ \end{Bmatrix} = \begin{bmatrix} \cos\bar{\alpha} & \sin\bar{\alpha} \\ -\sin\bar{\alpha} & \cos\bar{\alpha} \end{bmatrix} \begin{bmatrix} u \\ v \end{bmatrix}. \tag{23}$$

6. RESULTS

Fundamental experiments are performed in the Purdue Research Axial Fan Stage directed at investigating the aerodynamic forcing functions generated by an IGV row, both vortical and potential, including interactions with the downstream rotor. Data are acquired at an IGV outlet Mach number of 0·29 and a rotor relative inlet Mach number of 0·6. These data define the IGV wake upstream and downstream of the rotor for three IGV-rotor axial spacings, $Z/C_R = 0{\cdot}68$, 0·93, and 1·18.

6.1. Inlet Guide Vane Wake Correlations

IGV wake data for the three IGV-rotor axial spacings are compared with the empirical Majjigi & Gliebe correlations for the semiwake width δ and the wake centerline velocity defect W_{dc}. Figure 2 shows the measured IGV wake velocity as a function of tangential location across one blade passage. Note the asymmetric shape of this wake. It results from the boundary layer on the suction surface being larger than that on the pressure surface (Lakshminarayana & Davino 1980). This asymmetric characteristic dictates that the semi-wake width be calculated as the sum of two contributions from each side of the centerline, one from the suction side of the wake and the other from the pressure side of the wake (Majjigi & Gliebe 1984). Note that Figure 2 only shows the wake velocity deficit for the pressure surface side.

The measured wake velocity deficit exhibits poor agreement to the correlation in the near-field region, which is similar to results for the rotor blade wakes (Johnston *et al.* 1994). IGV-rotor axial spacing changes have no effect on the wake velocity deficit for the two

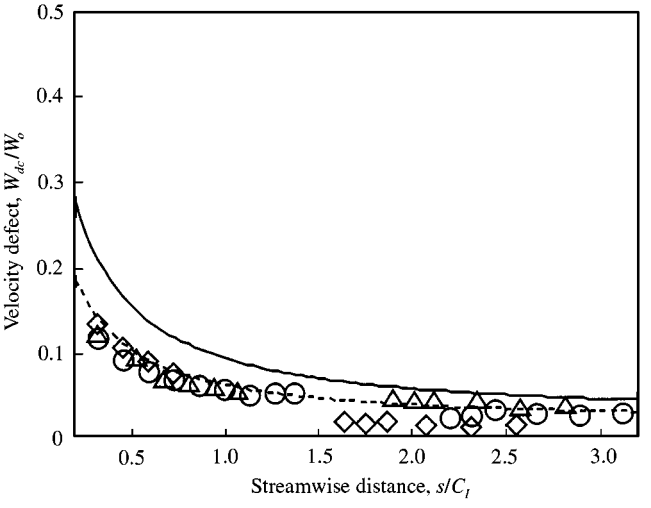

Figure 4. IGV-rotor spacing effect on the velocity-deficit correlation for $M_r = 0{\cdot}29$: ○, $Z/C_R = 1{\cdot}18$; △, $Z/C_R = 0{\cdot}93$; ◇, $Z/C_R = 0{\cdot}68$; ——, Majjigi–Gliebe correlation; ------, modified Majjigi–Gliebe correlation.

largest IGV-rotor spacings and lead to smaller deficits downstream of the rotor for the smallest spacing. The correlation for W_{dc}/W_o yields a standard deviation from the data of 0·023 and normalized standard deviation of 17·1%. This large discrepancy between the correlation and the experimental values for the W_{dc}/W_o are attributed to the poor data-correlation agreement in the near-IGV trailing edge region. Plotting the Majjigi & Gliebe correlation using a drag coefficient, which is 20% of the tabulated value, is shown in Figure 4. This modified curve fit gives a normalized standard deviation of 7·4%.

In the near-IGV wake region, the measured semi-wake width δ is always less than that predicted by the correlation (Figure 5). In the far-wake region, the disagreement between semi-wake width data and the empirical correlation becomes greater. The far-field wake has passed through the rotor that appears to reduce the rate at which the semi-wake width increases. IGV-rotor axial spacing changes have minimal effect on the semi-wake width upstream of the rotor for the three spacings tested. For the δ/C_I correlation, the standard deviation from the data is 0·03 and the maximum value of the y coordinate is 0·18 which yields a normalized standard deviation of 16·7%. A modified Majjigi & Gliebe correlation that utilizes a drag coefficient that is 20% of the tabulated value for this airfoil section is shown in Figure 5. The modification was chosen because it gave a good agreement when used in the Majjigi–Gliebe velocity deficit correlation. This modified curve fit gives a normalized standard deviation of 12·5%.

Data for the semi-wake width agree with the saturation growth rate equation and are shown in Figure 6. The saturation–growth rate equation, equation (24), usually characterizes population growth rate under limiting conditions:

$$\frac{\delta}{C_I} = \frac{0{\cdot}254(s/C_I)C_d^{0{\cdot}125}}{0{\cdot}9252 + (s/C_I)C_d^{0{\cdot}125}}. \tag{24}$$

This is a nonlinear relationship between the dependent and independent variables that levels off, or saturates as the independent variable increases. Good agreement to this curve fit exists in both the near- and far-fields, regardless of the fact that the wakes pass through

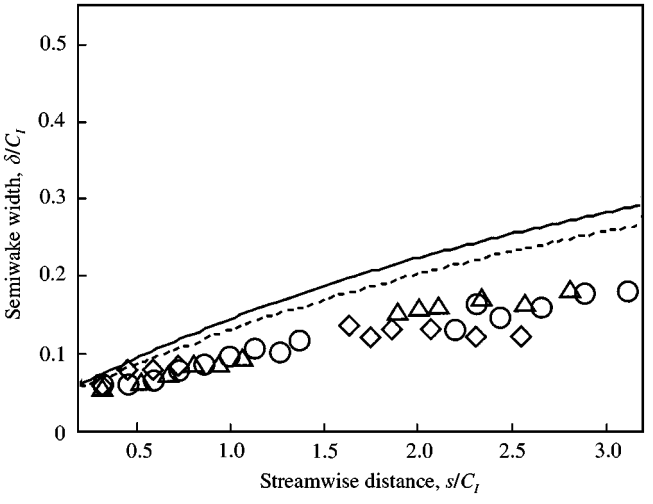

Figure 5. IGV-rotor spacing effect on semi-wake width correlation for $M_r = 0{\cdot}29$: ○, $Z/C_R = 1{\cdot}18$; △, $Z/C_R = 0{\cdot}93$; ◇, $Z/C_R = 0{\cdot}68$; ——, Majjigi–Gliebe correlation; ------, modified Majjigi–Gliebe correlation.

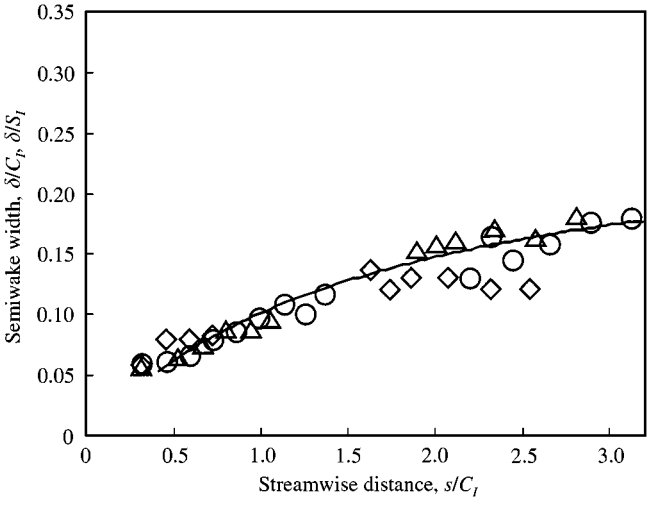

Figure 6. Semi-wake width for three IGV-rotor spacings compared with saturation–growth-rate equation for $M_r = 0{\cdot}29$: ○, $Z/C_R = 1{\cdot}18$; △, $Z/C_R = 0{\cdot}93$; ◇, $Z/C_R = 0{\cdot}68$; ——, equation (24).

the rotor. The standard deviation of the data from the correlation is 0·01 and the normalized standard deviation is 5·6%.

6.2. Vortical–Potential Gusts

With positive pressure variations plotted to the left, Figure 7 shows the velocity and static pressure spatial perturbations for the maximum IGV-rotor axial spacing at nine axial locations upstream and six axial locations downstream of the rotor. The axial and tangential coordinates are nondimensionalized by the characteristic length for the wake analysis,

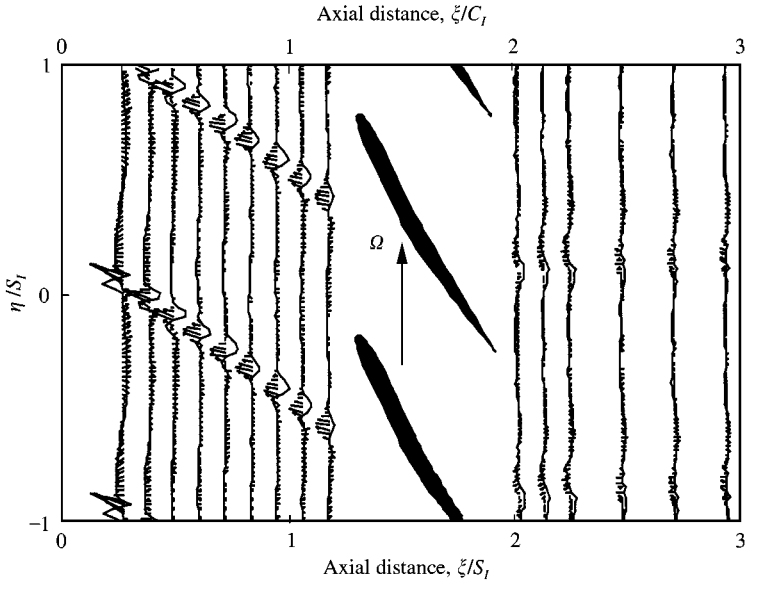

Figure 7. IGV-generated unsteady flow field upstream and downstream of the rotor.

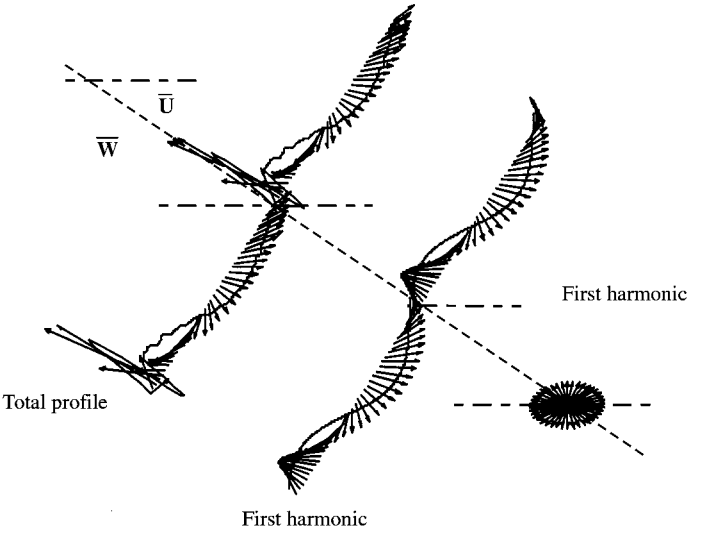

Figure 8. Measured gust immediately downstream of the IGV; $\frac{w_m^+}{\bar{U}} = 0{\cdot}029 \angle -176{\cdot}1^\circ$, $\frac{v_m^+}{\bar{U}} = 0{\cdot}026 \angle -67{\cdot}1^\circ$, $\frac{u_m^+}{v_m^+} = 1{\cdot}12 \angle -64{\cdot}1^\circ$.

the IGV vane-to-vane spacing S_I. The axial coordinate origin is the IGV trailing edge at midspan.

The velocity and pressure spatial perturbations clearly indicate the narrow viscous wakes emanating from the IGV trailing edges. The spatially unsteady static pressure perturbations in the wakes downstream of the IGV row are calculated from the total pressure and velocity

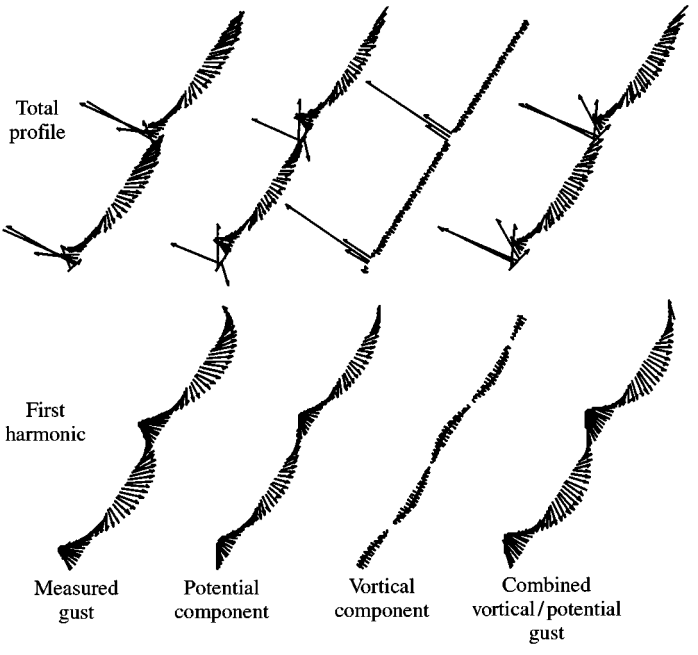

Figure 9. Splitting analysis applied to gust immediately downstream of the IGV; $A_1^* = 0{\cdot}0188 \angle 96{\cdot}5^\circ$, $D_1^* = 0{\cdot}0114 \angle -153{\cdot}6^\circ$.

measurements using isentropic relations. Note that the velocity vectors and pressure curves have been normalized by the mean flow velocity of the entire traverse which leads to the properties downstream of the rotor being scaled slightly larger because of the axial exit flow from the rotor.

Figure 8 shows the measured wake nearest the IGVs. Note that the gust wave number vector is a concept as valid for a stationary airfoil row as for a moving blade row. The gust plot is thus constructed along the wavenumber vector in a manner identical to that downstream of a rotor (Feiereisen *et al.* 1993). The spatial static pressure and velocity perturbations are both quite large. The magnitude and phase of the first-harmonic streamwise-to-transverse gust component ratio u_m^+/v_m^+ are 1·12 and $-64{\cdot}1^\circ$, respectively. Hence, the spatially unsteady velocity vector traces out a large oval and rotates clockwise.

The result of applying the splitting analysis to the data nearest the IGV is shown in Figure 9. The first-harmonic content of the vortical and potential gusts reveals that the first harmonic of the potential gust contains most of the information in the complete potential gust, but the vortical gust has significant contributions from the higher harmonics.

Figure 10 shows the vortical gust calculated from the splitting analysis as it convects downstream and passes through the rotor. The vortical gust has large narrow perturbations in the near-wake region that is indicative of contributions from harmonics higher than the first.

6.3. Axial Gust Behavior

The axial behavior of the first-harmonic potential gust component calculated by the splitting analysis and specified by the value of A_1^* for the largest IGV-rotor spacing is shown in Figure 11. The theory line is calculated by decaying the first value of A_1^* at the rate

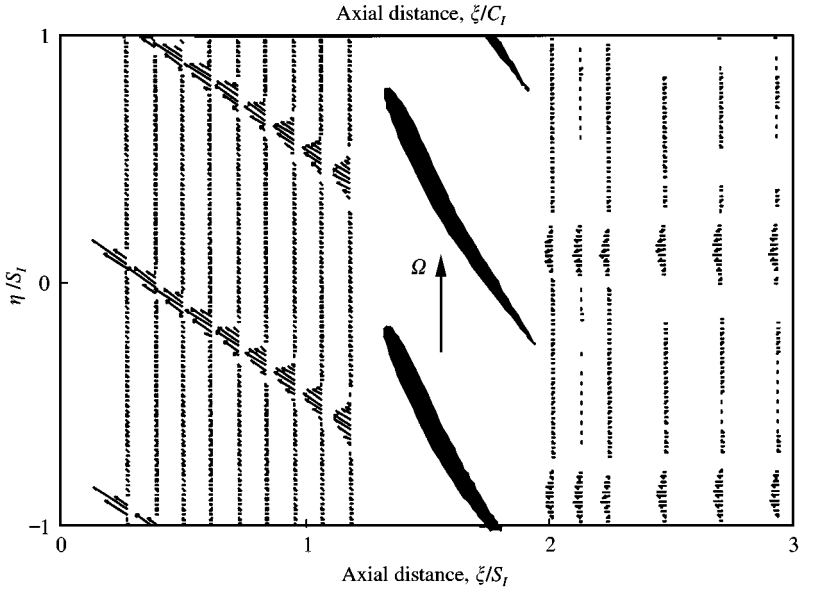

Figure 10· IGV wake vortical component upstream and downstream of the rotor.

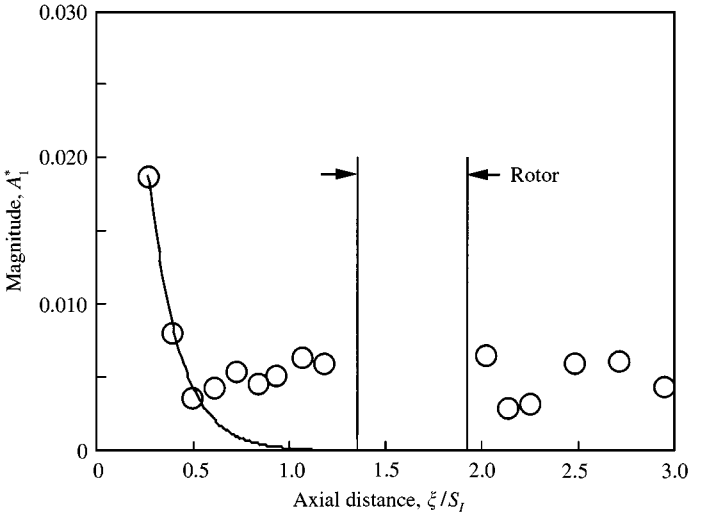

Figure 11. Axial behavior of the potential gust component: ——, theory; ○, $Z/C_R = 1{\cdot}18$.

predicted by the theory. Potential effects are quite strong immediately downstream of the IGV row. They initially decay, in agreement with theory. Once the value of the magnitude of A_1^* reaches 0·005, the potential component no longer decays, but remains approximately at this value even after the gust passes through the rotor.

Figure 12 shows the axial behavior of the rotor wake first-harmonic vortical gust component calculated by the splitting analysis and specified by the value of the magnitude of the vortical gust constant D_1^*. As predicted by the theory, D_1^* is relatively constant, although it has a slightly positive slope upstream of the rotor. There is a significant decrease

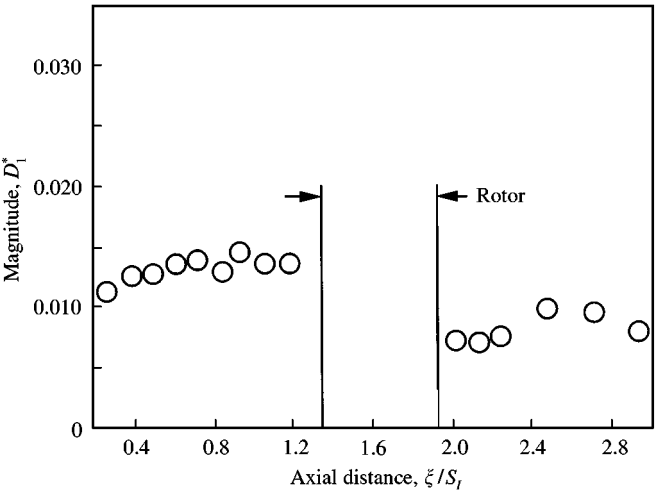

Figure 12. Axial behavior of the vortical gust component; ○, $Z/C_R = 1{\cdot}18$.

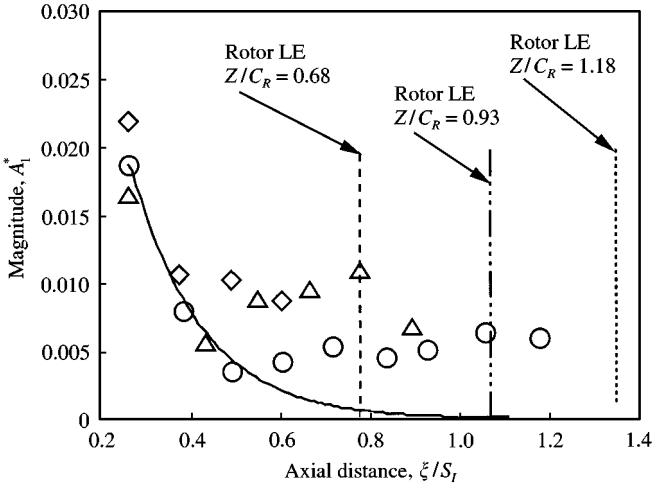

Figure 13. Axial behavior of the potential gust component upstream of the rotor: ——, theory; ○, $Z/C_R = 1{\cdot}18$; △, $Z/C_R = 0{\cdot}93$; ◇, $Z/C_R = 0{\cdot}68$;

in D_1 when the gust passes through the rotor, and it remains relatively constant downstream of the rotor.

The effect of the IGV-rotor axial spacing on the axial behavior of the rotor nondimensional first-harmonic vortical and potential gust components, specified by D_1^* and A_1^*, are shown in Figures 13–16. The magnitude of D_1^* is relatively constant both upstream and downstream of the rotor, as predicted by the theory. The results for D_1^* from all IGV-rotor axial spacings are in agreement. Decreasing the IGV-rotor spacing has a considerable effect on the potential gust constant A_1^*. In the rotor near-field upstream of the rotor, the magnitude of A_1^* increases with the decrease in the IGV-rotor axial spacings. Note that the theory predicts the farfield potential gust decays to zero while the data do not.

That drag force on the surface of an IGV and separation from the IGV surface lead to losses in total pressure is well known. A fact not well known is that viscous wakes can have

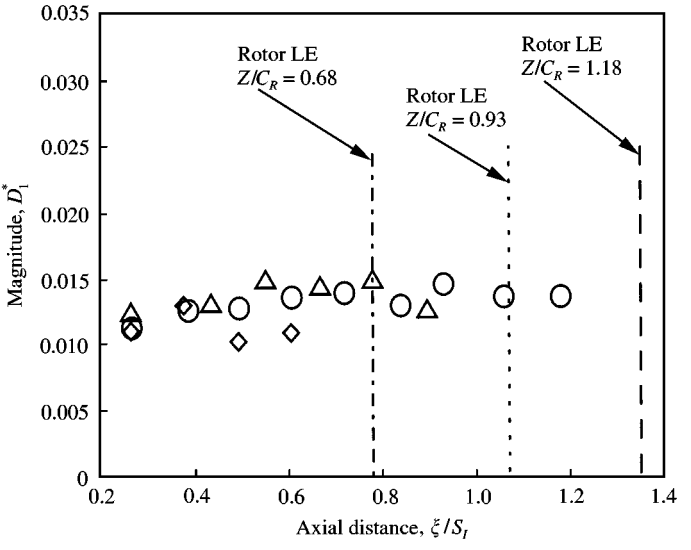

Figure 14. Axial behavior of the vortical gust component upstream of the rotor: ○, $Z/C_R = 1{\cdot}18$; △, $Z/C_R = 0{\cdot}93$; ◇, $Z/C_R = 0{\cdot}68$.

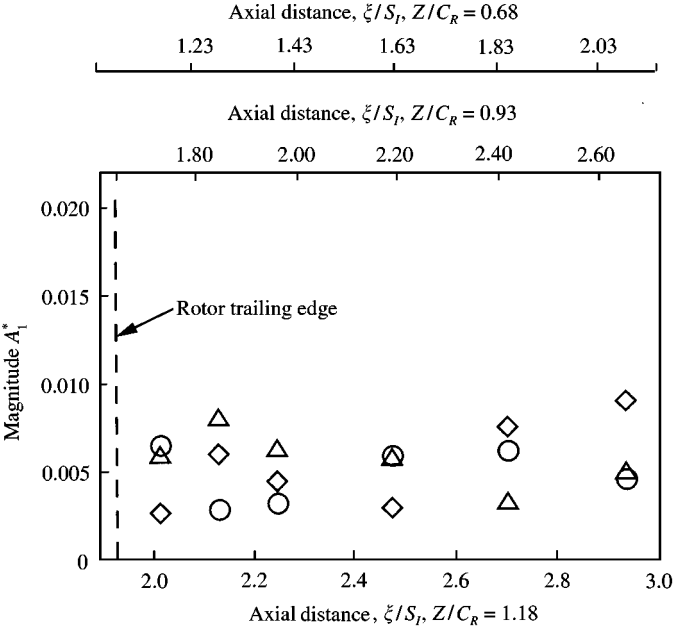

Figure 15. Axial behavior of the potential gust component downstream of the rotor: ○, $Z/C_R = 1{\cdot}18$; △, $Z/C_R = 0{\cdot}93$; ◇, $Z/C_R = 0{\cdot}68$.

static pressure variations. Cumpsty (1989) states in his discussion of special problems of viscous flow in compressors that large total pressure gradients can exist in all directions and as a result the static pressure is not constant in the viscous region. The vanes are highly cambered and were operated at a high stagger angle (21°) that increases the total pressure

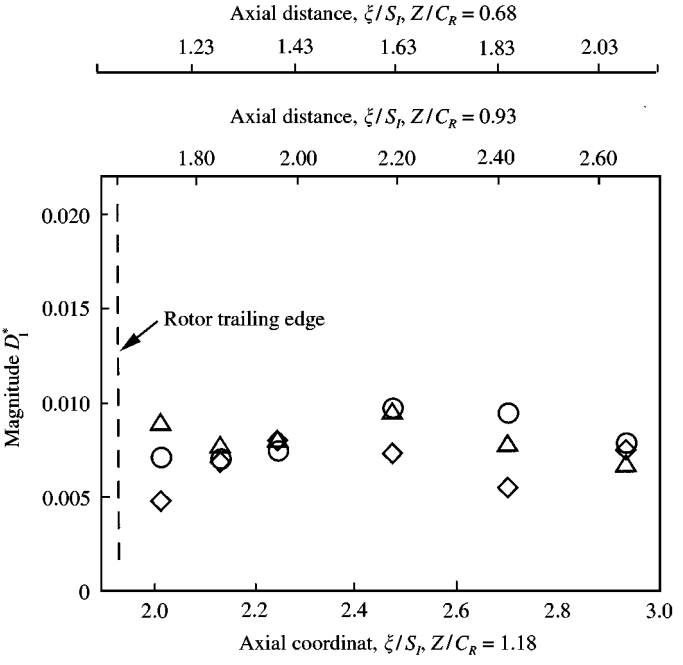

Figure 16. Axial spacing effect on the vortical gust axial variation downstream of the rotor: ○, $Z/C_R = 1{\cdot}18$; △, $Z/C_R = 0{\cdot}93$; ◇, $Z/C_R = 0{\cdot}68$.

losses. Tapered and twisted vanes are expected to create higher gradients in the flow properties than vanes with minimal twist and constant chord. This phenomenon could explain why the potential gust does not decay to zero as expected for an inviscid flow. Great care was taken in placing the probe into the test-section in order to minimize any misalignment between the total pressure and velocity profiles. Measurements at the minimum IGV-rotor spacing were taken with a static pressure probe and the calculated values of A_1^* were in agreement with those presented in this investigation. Propagating acoustic modes which vary in magnitude with IGV position due to the IGV-rotor–support strut interaction may also be a contributing factor to this nonzero potential (Schmidt & Okiishi 1977; Walker & Oliver 1972).

Since the total vortical gust has a large contribution from higher harmonics, it is important to consider the axial behavior of these components. Upstream of the rotor, the magnitude of the first three harmonics remain relatively constant, while the magnitude of the fourth and higher components decay at a nearly uniform rate for the largest IGV-rotor spacing, Figure 17. These higher harmonics (above the third) decay as a result of viscous diffusion that would not be present were the flow inviscid. A slight increase in the first-harmonic magnitude of the gust as it approaches the rotor can be explained as energy being transferred from the higher harmonics to the lower harmonics as the wakes decay. The slope of the seventh harmonic was measured to be 0·0067. After the IGV wakes pass through the rotor, the first five harmonics are still apparent and remain constant with axial location but are significantly reduced in magnitude. Harmonics above the fifth are reduced to zero by the action of the rotor. The decay of the harmonics of the vortical gust for the smaller two spacings is similar to the results found at the largest IGV-rotor spacing.

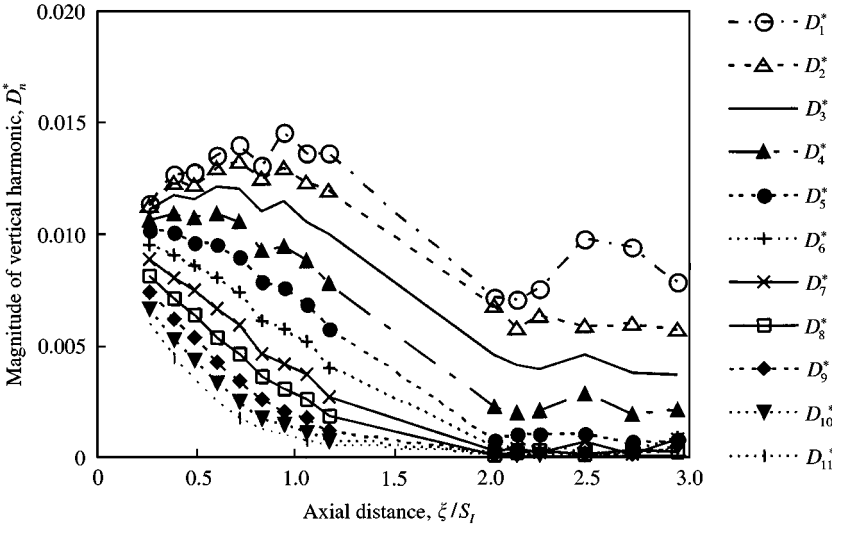

Figure 17. Vortical component higher harmonic axial decay ($Z/C_R = 1{\cdot}18$)

7. SUMMARY AND CONCLUSIONS

Fundamental experiments were performed in the Purdue Research Axial Fan Stage directed at investigating the aerodynamic forcing functions generated by an IGV row, both vortical and potential, including interactions with the downstream rotor. Data were acquired at an IGV outlet Mach number of 0·29 and a rotor relative inlet Mach number of 0·6. These data defined the IGV wake upstream and downstream of the rotor for three IGV-rotor axial spacings, $Z/C_R = 0{\cdot}68$, 0·93 and 1·18.

The vortical and potential forcing functions for the IGV wakes were studied as the wakes decayed and then passed through the rotating blade row. Forcing functions from the stationary IGV row were apparent upon passing through rotating blade rows and could impact the behavior of downstream airfoil rows. The spatial velocity and pressure perturbations were largest just downstream of the IGV row and decayed with distance travelled. Downstream of the rotor, the IGV wakes were still evident but are significantly reduced in extent.

With regard to the comparison of the IGV semi-wake width data with the empirical Majjigi & Gliebe correlations, differences in the near-wake region were noticeable, with even larger discrepancies from the correlation in the far field. These discrepancies in the semi-wake width are attributed to several factors. Unlike the rotor blade, an IGV is highly cambered and twisted; the unsteady flow field of the rotor could act to reduce the losses on the IGVs; also, the streamline curvature effects would not be present in measurements taken in a cascade; and, most importantly, the wakes have convected through a moving rotor in this study. Measured IGV wake velocity deficits agreed with the trends of empirical correlations and, using a drag coefficient that was 20% of the tabulated value for this airfoil section, yielded good agreement.

The IGV-rotor axial spacing variations of these experiments had minimal effect on the IGV wake velocity deficit or the semi-wake width when the wakes were upstream of the rotor. However, the IGV wakes were significantly reduced at the minimum IGV-rotor spacing.

Application of the splitting analysis showed that the gust has both a large potential and vortical content immediately downstream of the IGVs. Upstream of the rotor, D_1^* is relatively unchanged with the decreasing IGV-rotor spacing. The magnitude of D_1^* decreases when the gust propagates through the rotor and then remains relatively constant as it convects downstream of the rotor. Decreasing the IGV-rotor axial spacing resulted in minimal change of the magnitude of the vortical gust constant D_1^*. The harmonics of the vortical gust greater than the third harmonic decayed at a nearly constant rate upstream of the rotor while the first three harmonics remained relatively constant. The higher harmonics decayed due to viscous effects and the slight increase in the first harmonic with axial distance upstream of the rotor was attributed to energy being transferred from higher harmonics to the lower ones for the maximum spacing. It may be useful to characterize the decay of isolated vane wakes by the decay of the harmonics of the vortical component. Downstream of the rotor, the vortical gust is composed of the first five harmonics with all harmonics greater than five reduced to zero. The first two harmonics of the IGV vortical gust downstream of the rotor remained constant in magnitude.

For the largest IGV-rotor spacing, the magnitude of A_1^* decays according to the theoretical predictions until it reaches a value of approximately 0·005. The potential component then no longer decays but fluctuates about this minimum. Upstream of the rotor, in the rotor near-field, the potential gust constant A_1^* increased as the IGV-rotor spacing decreased. Total pressure gradients and variation in the magnitude of the propagating acoustic modes due to traversing the IGV row were determined to be responsible for the nonzero potential component in the far field.

ACKNOWLEDGMENTS

This research was sponsored by the GUIde Consortium on Bladed Disk Forced Response and is most gratefully acknowledged.

References

Cumpsty, N. A. 1989 *Compressor Aerodynamics*, New York: Longman Scientific & Technical, copublished by John Wiley and Sons, Inc. pp. 312–313.

Feiereisen, J. M., Montgomery, M. D. & Fleeter, S. 1993 Unsteady aerodynamic forcing functions: a comparison between linear theory and experiment. *ASME Paper* 93-*GT*-141.

Goldstein, M. E. 1978 Unsteady vortical and entropic distortions of potential flows round arbitrary obstacles. *Journal of Fluid Mechanics* **89,** 433–468.

Henderson, G. H. & Fleeter, S. 1992 Forcing function effects on unsteady aerodynamic gust response part 1: forcing functions. ASME Paper 92-GT-174.

Johnston, R. T., Feiereisen, J. M. & Fleeter, S. 1994 Rotor wake and potential forcing functions, including blade row interactions. 30*th Joint Propulsion Conference*, AIAA Paper No. 94-2975.

Lakshminarayana, B. & Davino, R. 1980 Mean velocity and decay characteristics of the guide vane and stator blade wake of an axial flow compressor. *ASME Journal of Engineering for Power* **102,** 50–60.

Majjigi, R. K. & Gliebe, P. R. 1984 Development of a rotor wake/vortex model, Vol. 1—Final Report. *NASA Contract Report No. 174849*, pp. 6–21.

Manwaring, S. R. & Wisler, D. C. 1992 Unsteady aerodynamics and gust response in compressors and turbines. *ASME Paper 92-GT-422*.

Mugridge, B. D. & Morfey, C. L. 1971 Sources of noise in axial flow fans. *Journal of the Acoustical Society of America* **51,** 1411–1426.

Schmidt, D. P. & Okiishi, T. H. 1977 Multistage axial-flow turbomachine wake production, transport, and interaction. *AIAA Journal* **15,** 1138–1145.

Walker, G. J. & Oliver, A. V. R. 1972 The effect of interaction between wakes from blade rows in an axial flow compressor on the noise generated by blade interaction. *ASME Journal of Engineering for Power*, **94,** 241–248.

APPENDIX: NOMENCLATURE

A_n	potential disturbance nth-harmonic proportionality constant
D_n	vortical disturbance nth-harmonic proportionality constant
C_I	IGV chord
C_R	rotor chord
$\mathbf{k}$	gust wavenumber vector
M	Mach number
p	static pressure perturbation
s	streamwise distance from rotor trailing edge
S_I	IGV spacing
S_R	rotor blade spacing
u	axial velocity perturbation
u^+	streamwise velocity perturbation
$\bar{\mathbf{U}}$	mean absolute velocity vector
$\mathbf{U}$	absolute velocity vector
v	tangential velocity perturbation
v^+	transverse velocity perturbation
$\mathbf{w}$	perturbation velocity vector
$\mathbf{W}$	mean IGV-relative velocity vector
W_{dc}	wake streamwise centerline velocity defect
W_{o}	free-stream streamwise velocity
δ	semi-wake width
ϕ_p	unsteady potential
$\bar{\rho}$	mean density
ξ	axial downstream distance measured from IGV trailing edge
η	tangential direction

Subscripts

c	combined vortical/potential
m	measured
p	potential
v	vortical
R	rotor
I	IGV